

CD-GAN: a robust fusion-based generative adversarial network for unsupervised change detection between heterogeneous images

Jin-Ju Wang, Nicolas Dobigeon, Marie Chabert,
Ding-Cheng Wang, Jie Huang and Ting-Zhu Huang

Abstract

In the context of Earth observation, the detection of changes is performed from multitemporal images acquired by sensors with possibly different characteristics and modalities. Even when restricting to the optical modality, this task has proved to be challenging as soon as the sensors provide images of different spatial and/or spectral resolutions. This paper proposes a novel unsupervised change detection method dedicated to such so-called heterogeneous optical images. This method capitalizes on recent advances which frame the change detection problem into a robust fusion framework. More precisely, we show that a deep adversarial network designed and trained beforehand to fuse a pair of multiband images can be easily complemented by a network with the same architecture to perform change detection. The resulting overall architecture itself follows an adversarial strategy where the fusion network and the additional network are interpreted as essential building blocks of a generator. A comparison with state-of-the-art change detection methods demonstrate the versatility and the effectiveness of the proposed approach.

Index Terms

Heterogeneous change detection, generative adversarial network (GAN), fusion.

Part of this work has been supported by the ANR-3IA Artificial, Natural Intelligence Toulouse Institute (ANITI) under grant agreement ANITI ANR-19-PI3A-0004, NSFC (Grant No. 12171072), Key Projects of Applied Basic Research in Sichuan Province (Grant No. 2020YJ0216), and National Key Research and Development Program of China (Grant No. 2020YFA0714001).

Jin-Ju Wang, Ding-Cheng Wang, Jie Huang, and Ting-Zhu Huang are with School of Mathematical Sciences, University of Electronic Science and Technology of China (UESTC), Chengdu, Sichuan, China (e-mail: jinjuwang123@163.com, wangdc@uestc.edu.cn, huangjie_uestc@uestc.edu.cn, and tingzhuhuang@126.com).

Nicolas Dobigeon and Marie Chabert are with the University of Toulouse, IRIT/INP-ENSEEIH, 31000 Toulouse, France (e-mail: {nicolas.dobigeon, marie.chabert}@enseiht.fr).

Nicolas Dobigeon is also with the Institut Universitaire de France (IUF), France.

I. INTRODUCTION

Change detection (CD) aims at identifying spatial areas affected by information alterations between two images acquired over the same scene but at different time instants [1], [2]. With the rapid development of urban areas and the frequent occurrence of natural disasters such as floods and earthquakes, CD has become an essential task to monitor land cover evolution [3]–[6].

Depending on the pair of sensors acquiring the two images under consideration, CD methods can be divided into homogeneous CD and heterogeneous CD [7]. Specifically, homogeneous CD identifies changes between images provided by sensors with same characteristics. In particular, when analyzing optical images, they are assumed to share the same spectral and spatial resolutions. The pipeline of most of the conventional homogeneous CD methods generally consists of three steps: image pre-processing, change image (CI) generation and binary change map (CM) generation [8]. More precisely, image processing aims at ensuring that the so-called homologous pixels in the pre-change and post-change images refer to the same spatial location. The second step generates CI by comparing the pre-processed images to highlight the changed areas. In the last step, high level processing such as segmentation or classification is conducted on the CI to label the pixels and/or group of pixels affected by changes.

This paper focuses on a more challenging CD applicative scenario that involves optical images of possibly different spatial and spectral resolutions. This scenario becomes more frequent due to the rapid development of remote sensing technologies. Indeed there is a growing availability of images coming from different sources (i.e., acquired by sensors with distinct specifications), which offers new opportunities to perform timely CD, especially in emergency cases, provided dedicated heterogeneous CD methods are specifically designed. As an archetypal scenario considered for illustrative purpose in this paper, heterogeneous CD may involve a pair of images of complementary resolutions, i.e., a high spatial but low spectral resolution (HRLS) image and a low spatial but high spectral resolution (LRHS) image. For instance, adopting a conventional dichotomy over the optical sensors, this leads to consider a pair of panchromatic (PAN) and multispectral (MS) images, a pair of PAN and hyperspectral (HS) images or a pair of MS and HS images. When facing to this diversity of spatial and spectral resolutions, the conventional CD pipeline briefly outlined above is inapplicable since homologous pixels cannot be directly compared. To address this issue, various strategies have been proposed [9]–[13], which mainly rely on individual transformation-based techniques to make this subsequent comparison possible. These transformations basically embed the HRLS and LRHS images into an identical feature space where they can be compared using conventional homogeneous CD methods [14], [15]. Especially, to generate a pair of images with the same spatial and spectral resolutions, interpolation and resampling are classically used [16], [17]. For instance, a pair of HRLS images

are obtained by simultaneously implementing spatial interpolation and spectral down-sampling on the LRHS images. However, the above strategies consider each image individually without jointly exploiting their respective yet shared spatial and spectral information.

Instead of individually pre-processing the observed images, a general CD framework introduced in [18] and extended in [19], [20] tackles the CD problem as a multiband image fusion task. To fully and jointly exploit the spatial and spectral information brought by the pair of observed images, a latent (i.e., unobserved) image is inferred as a fused product. While avoiding to spatially and/or spectrally degrade the observed images, this fusion process allows a CD map to be subsequently recovered with the best spatial and spectral resolutions. This strategy shows to outperforms state-of-the-art CD methods relying on transform-based techniques.

Meanwhile, some recent works exploit the versatility of deep neural networks to perform CD between homogeneous or heterogeneous images [12], [21]–[23]. For instance, in [24], new cycle-consistent adversarial networks (CycleGANs) are proposed to learn the subimage-to-subimage mapping using given pairs of pre-change and post-change images. Then, using the trained CycleGANs, LRHS images are translated into a common space (i.e., associated with HRLS images). However, most of these deep architectures are designed to perform supervised CD, i.e., their training requires a learning database of pairs of images with annotated changes.

This paper capitalizes on the fusion-based CD framework proposed in [20] while simultaneously leveraging on recent advances on deep learning-based fusion to perform unsupervised CD, i.e., without assuming the prior availability of pairs of images with annotated changes. More precisely, we reformulate the inference of the CI as a generation task within an adversarial framework. We show that any pretrained generative fusion network of the literature can then serve as an essential building block of the underlying strategy. The resulting architecture is a specific instance of generative adversarial networks (GAN), firstly introduced by Goodfellow *et al.* [25] and popularized by their success in various applications [26], [27]. When compared to more conventional model-based approaches, thanks to the versatility of neural networks, the strategy adopted in this paper appears to be much more flexible since it may easily depart from simplifying assumptions initially formulated in the former contributions.

This article is organized as follows. Section II recalls how the problem of CD can be cast as a robust fusion task. Capitalizing on this formulation, an adversarial framework is proposed in Section III and a possible architecture is detailed for the particular case of complementary acquisitions. Experimental results obtained on simulated data sets are reported in Section IV to assess the efficiency, the versatility and the robustness of the proposed approach when compared to alternative CD methods. Section V illustrates the relevance approach when analyzing real data sets. Finally, Section VI concludes the paper.

II. BACKGROUND: ROBUST FUSION-BASED CHANGE DETECTION

This paper focuses on the problem of detecting changes between two optical images denoted $\mathbf{Y}_1 \in \mathbb{R}^{m_1 \times n_1}$ and $\mathbf{Y}_2 \in \mathbb{R}^{m_2 \times n_2}$, respectively, acquired over the same scene but at different times t_1 and t_2 by two sensors \mathbf{S}_1 and \mathbf{S}_2 . Here, the quantities m_i and n_i stand for the number of bands and the number of pixels of the image \mathbf{Y}_i ($i \in \{1, 2\}$), respectively. In the context of heterogeneous CD, the two images are assumed to be of different spatial and/or spectral resolutions, i.e., $n_1 \neq n_2$ and/or $m_1 \neq m_2$.

Remark 1 (Complementary acquisitions) *Throughout this paper, for an illustrative purpose but without loss of generality, we will consider the particular case of images characterized by complementary resolutions, as in [19]. This can be stated by the following relations*

$$m_1 \geq m_2 \text{ and } \Delta n = n_2/n_1 \quad (1)$$

where $\Delta n \geq 1$ is the product of the spatial decimation factors in the horizontal and vertical directions. In other words, \mathbf{Y}_1 and \mathbf{Y}_2 are LRHS and HRLS images, respectively. It is worth noting that other applicative scenarios listed in [19] can be easily handled following the approach detailed in the following paragraphs.

Because of these different spatial and/or spectral resolutions, a pairwise comparison of the pixels in \mathbf{Y}_1 and \mathbf{Y}_2 cannot be conducted to locate the changes. To overcome this difficulty, the adversarial strategy proposed in this paper elaborates on the robust fusion framework proposed in [19] and generalized in [20]. This framework proposes to relate the two observed images \mathbf{Y}_1 and \mathbf{Y}_2 to two latent images $\mathbf{X}_1 \in \mathbb{R}^{m \times n}$ and $\mathbf{X}_2 \in \mathbb{R}^{m \times n}$ of same spatial and spectral resolutions through the observation models

$$\mathbf{Y}_1 = \mathcal{H}_1(\mathbf{X}_1) \quad (2a)$$

$$\mathbf{Y}_2 = \mathcal{H}_2(\mathbf{X}_2) \quad (2b)$$

where $\mathcal{H}_1 : \mathbb{R}^{m \times n} \rightarrow \mathbb{R}^{m_1 \times n_1}$ and $\mathcal{H}_2 : \mathbb{R}^{m \times n} \rightarrow \mathbb{R}^{m_2 \times n_2}$ stand for degradation operators, respectively. These operators are assumed to be linear, i.e., $\mathcal{H}_i(\mathbf{A} + \lambda\mathbf{B}) = \mathcal{H}_i(\mathbf{A}) + \lambda\mathcal{H}_i(\mathbf{B})$ for $i \in \{1, 2\}$ and $\lambda \in \mathbb{R}$. In the general case, the latent space $\mathbb{R}^{m \times n}$ where the latent images \mathbf{X}_1 and \mathbf{X}_2 live is such that $n \geq \max\{n_1, n_2\}$ and $m \geq \max\{m_1, m_2\}$, reflecting the fact that these latent images are of resolutions at least of those defining the observed images.

Remark 2 (Complementary acquisitions) *In case of complementary acquisitions, the operators $\mathcal{H}_1(\cdot)$ and $\mathcal{H}_2(\cdot)$ stand for spatial and spectral degradations, respectively. In [19], as in most of*

the fusion works of the literature dealing with multiband imaging [28]–[32], they are defined as

$$\mathcal{H}_1(\mathbf{X}) \approx \mathbf{X}\mathbf{R},$$

$$\mathcal{H}_2(\mathbf{X}) \approx \mathbf{L}\mathbf{X},$$

where the right-side multiplication matrix \mathbf{R} is generally decomposed as $\mathbf{R} = \mathbf{B}\mathbf{S}$ with a spatially-invariant blurring matrix \mathbf{B} and a subsampling matrix \mathbf{S} and the left-side multiplication matrix \mathbf{L} is a spectral degradation specified by the filters of the sensor. The approximation symbol \approx stands for any mismodeling and measurement noise. The latent space $\mathbb{R}^{m \times n}$ embeds the set of images whose spatial and spectral resolutions are defined by the LRHS and HRLS images respectively, i.e., $n = n_2$ and $m = m_1$.

Then, detecting the changes that occurred during the two acquisition time instants can be tackled as an inference problem referred to as robust fusion whose two main steps are detailed below.

A. CI inference step

If the latent images \mathbf{X}_1 and \mathbf{X}_2 were available, since they share the same spatial and spectral resolutions, a CI denoted $\Delta\mathbf{X} \in \mathbb{R}^{m \times n}$ of higher spatial and/or spectral resolutions could be easily derived by a crude pixel-wise difference, i.e.,

$$\Delta\mathbf{X} = \mathbf{X}_2 - \mathbf{X}_1. \quad (3)$$

Conventional homogeneous CD methods, such as change vector analysis (CVA) and its extensions [33], [34], can then be used to derive the binary CM from the CI $\Delta\mathbf{X} = [\Delta\mathbf{x}_1, \dots, \Delta\mathbf{x}_n]$. In its canonical formulation, CVA consists in computing the energy image $\mathbf{e} = [e_1, \dots, e_n] \in \mathbb{R}^n$ of the change where, for $i = 1, \dots, n$,

$$e_i = \|\Delta\mathbf{x}_i\|_2.$$

The components e_i of \mathbf{e} tend to small values for unchanged pixels whose indices are gathered in the set Ω_u while changed pixels indexed in Ω_c have larger values. Thus a natural decision rule consists in thresholding the energy change image, i.e., for $i = 1, \dots, n$,

$$i \in \begin{cases} \Omega_c & \text{if } e_i > \tau, \\ \Omega_u & \text{otherwise,} \end{cases} \quad (4)$$

where the threshold τ balances the trade-off between the probability of false alarm and the probability of detection and can be adjusted using dedicated method [35]. Then, the final binary CM $\mathbf{d} = [d_1, \dots, d_n] \in \{0, 1\}^n$ can be derived as

$$d_i = \begin{cases} 1 & \text{if } i \in \Omega_c, \\ 0 & \text{if } i \in \Omega_u. \end{cases} \quad (5)$$

B. Fusion step

Reciprocally, when the CI $\Delta\mathbf{X}$ is known and fixed, the latent images \mathbf{X}_1 and \mathbf{X}_2 can be inferred by solving a multiband image fusion problem. Indeed, adopting the formalism introduced in [19] and exploiting the identity (3) and the linearity of the degradation operators, the direct models (2) can be equivalently rewritten as

$$\mathbf{Y}_1 = \mathcal{H}_1(\mathbf{X}_1), \quad (6a)$$

$$\tilde{\mathbf{Y}}_2 = \mathcal{H}_2(\mathbf{X}_1), \quad (6b)$$

where¹

$$\tilde{\mathbf{Y}}_2 \triangleq \mathbf{Y}_2 - \mathcal{H}_2(\Delta\mathbf{X}), \quad (7)$$

is the so-called *corrected* image that would be acquired by the sensor \mathbf{S}_2 at time t_1 , i.e., before any change. From the set of equations (6), it clearly appears that recovering the latent image \mathbf{X}_1 from the observed and corrected images \mathbf{Y}_1 and $\tilde{\mathbf{Y}}_2$ is an image fusion task. The other latent image \mathbf{X}_2 can be subsequently derived from \mathbf{X}_1 and $\Delta\mathbf{X}$ using (3).

Remark 3 (Complementary acquisitions) *Fusing a pair of images of complementary acquisitions aims at recovering a latent image whose spatial and spectral resolutions are the best of those of the observed images. This problem has motivated a wide bunch of research works over the three last decades, specifically dealing with pansharpening when fusing PAN and MS images [36], hyperspectral pansharpening when fusing PAN and HS images [37] or multiband image fusion when fusing MS and HS images [38].*

It is worth noting that any fusion method should fulfill a consistency property. This property states that a well-designed fusion process should be reversible in the sense that the observed image is expected to be as close as possible to the image that would be obtained by applying the acquisition process to the estimated fused image $\hat{\mathbf{X}}_1$ [39]. In other words, the so-called *predicted* image that should be observed by the sensor \mathbf{S}_1 at time instant t_1 , denoted as $\hat{\mathbf{Y}}_1$ and defined by

$$\hat{\mathbf{Y}}_1 = \mathcal{H}_1(\hat{\mathbf{X}}_1) \quad (8)$$

is expected to be indistinguishable from the observed image \mathbf{Y}_1 . This property has motivated the fusion-based CD method proposed in [18]. It will be also resorted to design a discriminative network embedded in the proposed adversarial framework detailed in the next section.

¹In this paper, we decided to introduce the corrected image at time t_1 . Another possible choice consists in defining the corrected image $\tilde{\mathbf{Y}}_1 \triangleq \mathbf{Y}_1 + \mathcal{H}_1(\Delta\mathbf{X})$ that would have been acquired by the sensor \mathbf{S}_1 at time t_2 , i.e., after the changes occur. In this case the subsequent technical derivations should be adapted accordingly.

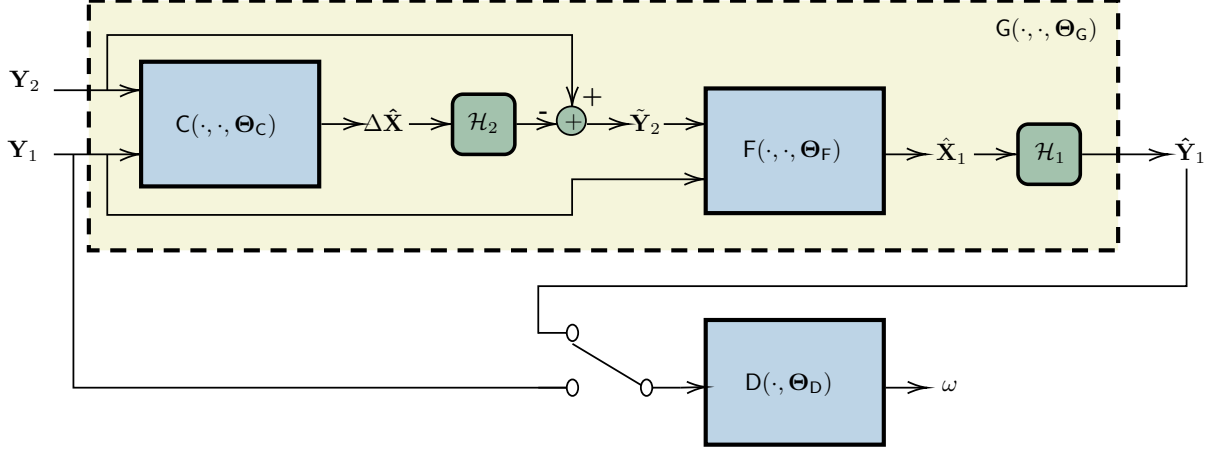


Fig. 1. Flowchart of the overall proposed CD-GAN architecture. The 3 main networks $C(\cdot, \cdot; \Theta_C)$, $F(\cdot, \cdot; \Theta_F)$ and $D(\cdot, \cdot; \Theta_D)$ appear as blue light boxes. The virtual generator $G(\cdot, \cdot; \Theta_G)$ is figured as a beige dashed-lined box.

III. PROPOSED ADVERSARIAL FRAMEWORK

The previous section showed that CD between heterogeneous images can be conducted by inferring a pair $\{X_1, X_2\}$ of latent images or, equivalently, a pair $\{X_1, \Delta X\}$ formed by one latent image and the CI with $X_2 = X_1 + \Delta X$. This inference problem, coined as robust fusion, can be solved using a procedure composed of two steps, namely CI inference and fusion, detailed in Sections II-A and II-B, respectively. Interestingly, we will show that these two tasks can naturally be embedded as essential building blocks into an adversarial architecture whose overall flowchart is depicted in Fig. 1. The different stages of this architecture, referred to as CD-GAN in the sequel, as well as the training strategy are detailed in this section. Finally, we provide a specific instance of this framework for the particular case of complementary acquisitions.

A. Overall architecture

First, CI inference can be interpreted as a mapping from the product set $\mathbb{R}^{m_1 \times n_1} \times \mathbb{R}^{m_2 \times n_2}$ of observed images towards the set $\mathbb{R}^{n \times m}$ of CIs. In this work, this unknown mapping is modeled as

$$\Delta \hat{X} = C(Y_1, Y_2; \Theta_C), \quad (9)$$

where $C(\cdot, \cdot; \Theta_C)$ is a deep network parameterized by Θ_C . It is clear from (9) that this network explicitly solves the problem of heterogeneous CD. Indeed, once trained, it directly provides as output the estimated CI $\Delta \hat{X}$ from which the binary change map \hat{d} can be retrieved as detailed in Section II-A. Second, adopting the notations introduced in the previous section, the fusion step can be formulated as a mapping from the product set $\mathbb{R}^{m_1 \times n_1} \times \mathbb{R}^{m_2 \times n_2}$ of observed images to the set $\mathbb{R}^{n \times m}$ of latent images, i.e.,

$$\hat{X}_1 = F(Y_1, \tilde{Y}_2; \Theta_F), \quad (10)$$

where $F(\cdot, \cdot; \Theta_F)$ stands for another network (or model-based fusion algorithm) parameterized by Θ_F . In this work, we propose to benefit from recent efforts promoting deep architectures specifically designed to solve the fusion task. Thus, in the sequel of the paper, we will assume that the fusion network $F(\cdot, \cdot; \Theta_F)$ has been previously trained, hence Θ_F is a set of fixed network parameters. It is worth noting that this fusion network implicitly requires the knowledge of the CI $\Delta\mathbf{X}$ or its estimate $\Delta\hat{\mathbf{X}}$ provided by the network $C(\cdot, \cdot; \Theta_C)$ since it takes as one input the corrected image $\tilde{\mathbf{Y}}_2$ defined by (7).

Training the network $C(\cdot, \cdot; \Theta_C)$ dedicated to the CI inference under an adversarial paradigm requires to design a suitable discriminator. One strategy would be to ensure that the fused image $\hat{\mathbf{X}}_1$ subsequently generated by the fusion network $F(\cdot, \cdot; \Theta_F)$ is in good agreement with the true latent image \mathbf{X}_1 . This is the training strategy generally adopted by most of the GAN-based fusion algorithms. However, this strategy requires a data set of pairs of fused and observed images, which could be difficult in practical scenarios. To lighten the supervision, we take a different route and propose a training strategy that only relies on the observed image \mathbf{Y}_1 . By leveraging on the consistency property of the fusion process and the expected characteristics of the predicted image $\hat{\mathbf{Y}}_1$ defined by (8), we propose to design a discriminative network which assesses the quality of the fusion network output as

$$\omega = D(\Upsilon; \Theta_D), \quad (11)$$

with $\Upsilon \in \{\mathbf{Y}_1, \hat{\mathbf{Y}}_1\}$ and where $\omega \in \{0, 1\}$ is the binary label stating the likelihood of the predicted image $\hat{\mathbf{Y}}_1$ with respect to (w.r.t.) the observed image \mathbf{Y}_1 and Θ_D is the set of network parameters to be trained.

To summarize, the overall proposed adversarial architecture can be decomposed into five main stages listed below

- *CI inference*: the generative network $C(\cdot, \cdot; \Theta_C)$ produces a candidate CI $\Delta\hat{\mathbf{X}}$ from the observed image \mathbf{Y}_1 and \mathbf{Y}_2 ,
- *Correction*: the candidate CI $\Delta\hat{\mathbf{X}}$ is used to produce the corrected image $\tilde{\mathbf{Y}}_2$ following (7),
- *Fusion*: the corrected image $\tilde{\mathbf{Y}}_2$ is subsequently fused with the observed image \mathbf{Y}_1 thanks to the already trained network $F(\cdot, \cdot; \Theta_F)$, providing the estimated latent image $\hat{\mathbf{X}}_1$,
- *Prediction*: the latent image $\hat{\mathbf{X}}_1$ allows the predicted image $\hat{\mathbf{Y}}_1$ to be computed following (8),
- *Discrimination*: the quality of the predicted image $\hat{\mathbf{Y}}_1$ is assessed w.r.t. the observed image \mathbf{Y}_1 thanks to the discriminative network $D(\cdot; \Theta_D)$.

It is worth noting that an alternate interpretation of the proposed architecture can be drawn by explicitly introducing a generator $G(\cdot, \cdot; \Theta_G)$ whose set of parameters writes $\Theta_G = \{\Theta_C, \Theta_F\}$. Since the fusion network is assumed to have been trained beforehand, this set of generator parameters

reduce to the parameters of the CI inference network, i.e., $\Theta_G = \Theta_C$. This generator, highlighted as a beige dashed-lined box in Fig. 1, takes as inputs the two observed images \mathbf{Y}_1 and \mathbf{Y}_2 and embeds the four first stages of the architecture to produce the predicted image $\hat{\mathbf{Y}}_1$, i.e.,

$$G(\mathbf{Y}_1, \mathbf{Y}_2; \Theta_C) \triangleq \hat{\mathbf{Y}}_1 = \mathcal{H}_1(\hat{\mathbf{X}}_1), \quad (12)$$

where we recall that

$$\begin{aligned} \hat{\mathbf{X}}_1 &= F(\mathbf{Y}_1, \tilde{\mathbf{Y}}_2; \Theta_F) \\ \tilde{\mathbf{Y}}_2 &= \mathbf{Y}_2 - \mathcal{H}_2(\Delta \hat{\mathbf{X}}) \\ \Delta \hat{\mathbf{X}} &= C(\mathbf{Y}_1, \mathbf{Y}_2; \Theta_C). \end{aligned}$$

Introducing this generator allows the proposed architecture to be cast into an (almost) canonical GAN framework², naturally yielding to a loss function specified in the next paragraph.

B. Loss function

In the proposed architecture, two networks need to be trained: the generative network $C(\cdot, \cdot; \Theta_C)$ and the discriminative network $D(\cdot; \Theta_D)$. Indeed, as stated before, the fusion network $F(\cdot, \cdot; \Theta_F)$ can be chosen as any state-of-the-art network (or even any model-based fusion algorithm) from the literature and it is thus assumed to have been previously trained (or calibrated). Suggested by the adversarial structure of the proposed architecture, the loss function derived in this work to train the two networks is composed of an adversarial term defined as

$$\mathcal{L}_{\text{adv}}(\Theta_C, \Theta_D) = \mathbb{E}_{\mathbf{Y}_1} [\log D(\mathbf{Y}_1; \Theta_D)] + \mathbb{E}_{\mathbf{Y}_1, \mathbf{Y}_2} [\log(1 - D(G(\mathbf{Y}_1, \mathbf{Y}_2; \Theta_C); \Theta_D))]. \quad (13)$$

As emphasized by previous works [26], it is often beneficial to enrich the adversarial cost with more application-oriented loss functions. Thus, the loss associated with the network $C(\cdot, \cdot; \Theta_C)$ dedicated to CI inference is complemented with two additional terms. First, the following prediction loss

$$\mathcal{L}_{\text{pre}}(\Theta_C) = \mathbb{E}_{\mathbf{Y}_1, \mathbf{Y}_2} [\|\mathbf{Y}_1 - \hat{\mathbf{Y}}_1\|_F^2], \quad (14)$$

is introduced to assess the quality of the predicted image $\hat{\mathbf{Y}}_1$ w.r.t. the actual image \mathbf{Y}_1 . Finally, since the changes are expected to affect only a few pixels (i.e., most of the columns of the CI are expected to be zero vectors), a spatial-sparsity inducing regularization is applied to the estimated CI

$$\mathcal{L}_{\text{spa}}(\Theta_C) = \mathbb{E}_{\mathbf{Y}_1, \mathbf{Y}_2} [\|\Delta \hat{\mathbf{X}}\|_{2,1}], \quad (15)$$

²A third and converse interpretation would consist in pipelining the four last stages of the architecture to define an extended discriminator combined with a generator defined as the sole network dedicated to the CI inference.

following the strategies already advocated in [19], [20]. Finally, training both networks boils down to solve the minimax problem

$$\min_{\Theta_C} \max_{\Theta_D} \mathcal{L}_{\text{adv}}(\Theta_C, \Theta_D) + \alpha \mathcal{L}_{\text{pre}}(\Theta_C) + \beta \mathcal{L}_{\text{spa}}(\Theta_C), \quad (16)$$

where α and β are hyperparameters adjusting the relative weights of the terms. In practice, following the common training procedures of GAN-based architectures, the two networks are alternately updated by stochastic gradient-based optimization, i.e., the expectations involved in the definition of the overall loss terms are approximated by empirical averages over minibatches.

Remark 4 (Interpreting the generator training) *Interestingly, the minimax optimization problem (16) underlying the training of the generative and discriminative networks can be straightforwardly interpreted from an image processing point-of-view. To easily draw this interpretation, let consider the deterministic setting or, equivalently, a minibatch composed of a unique sample. Under this simplified assumption, training the sole generative network $G(\cdot, \cdot; \Theta_G)$ dedicated to CI inference boils down to solve the optimization problem*

$$\min_{\Theta_C} \|\mathbf{Y}_1 - \hat{\mathbf{Y}}_1\|_F^2 + \|\Delta \hat{\mathbf{X}}\|_{2,1} + \mathcal{L}_{\text{adv}}(\Theta_C), \quad (17)$$

where the predicted image $\hat{\mathbf{Y}}_1$ and the CI $\Delta \hat{\mathbf{X}}$ implicitly depend on Θ_C . More precisely, by plugging the definition (8) of the predicted image $\hat{\mathbf{Y}}_1$, the loss function can be rewritten as

$$\min_{\Theta_C} \|\Delta \check{\mathbf{Y}}_1 - \mathcal{H}_1(\Delta \hat{\mathbf{X}})\|_F^2 + \|\Delta \hat{\mathbf{X}}\|_{2,1} + \mathcal{L}_{\text{adv}}(\Theta_C), \quad (18)$$

where $\check{\mathbf{Y}}_1 \triangleq \mathcal{H}_1(\mathbf{X}_2)$ is the image that would be virtually observed by the sensor \mathcal{S}_1 at time t_2 and $\Delta \check{\mathbf{Y}}_1 \triangleq \check{\mathbf{Y}}_1 - \mathbf{Y}_1$ is the predicted CI that would be obtained by differentiating the images virtually observed at time t_2 and actually observed at time t_1 by the sensor \mathcal{S}_1 . Since the CI $\Delta \hat{\mathbf{X}}$ is fully defined as the output of the network $C(\cdot, \cdot; \Theta_C)$ following (9), training this network by solving the nonlinear optimization problem (18) can be interpreted as a parametric inversion task: given the virtually observed CI $\Delta \check{\mathbf{Y}}_1$, one aims at inverting the measurement operator $\mathcal{H}_1(\cdot)$ by looking for a solution among a parametric family specified by Θ_C . It is worth noting that this inversion step has been explicitly referred to as a correction in [19], [20] where the adversarial term $\mathcal{L}_{\text{adv}}(\Theta_C)$ acts as an additional task-driven data fitting term.

C. Detailed architecture in case of complementary acquisitions

This section provides details on the network architectures for a specific instance of the proposed framework. More precisely, it considers the particular case of complementary acquisitions, i.e., when the observed images \mathbf{Y}_1 and \mathbf{Y}_2 are LRHS and HRLS images, respectively. As stated before, the fusion network $F(\cdot, \cdot; \Theta_F)$ can be chosen as any state-of-the-art architecture (or model-based algorithm) [29],

[31], [40]–[42] and is assumed to have been trained or calibrated beforehand. In this work, we adopt a network similar to the one introduced in [40], whose detailed architecture is depicted in Fig. 2. Specifically, the original-sized LRHS and HRLS images are provided as inputs of two sub-networks designed for feature extraction. These two sub-networks consist of two successive convolutional layers followed by a leaky rectified linear unit (LeakyReLU) [43] and a down-convolution layer. Since the spatial resolution of the LRHS image \mathbf{Y}_1 is lower than the one of the target latent image \mathbf{X}_1 , the second convolution layer of the dedicated sub-network is an up-convolution layer. The two resulting feature maps are then concatenated and pass through a pipeline of convolutional layers, complemented by U-Net like skip connections [44]. Finally, ReLU is applied in the last layer to ensure nonnegativity of the output fused image.

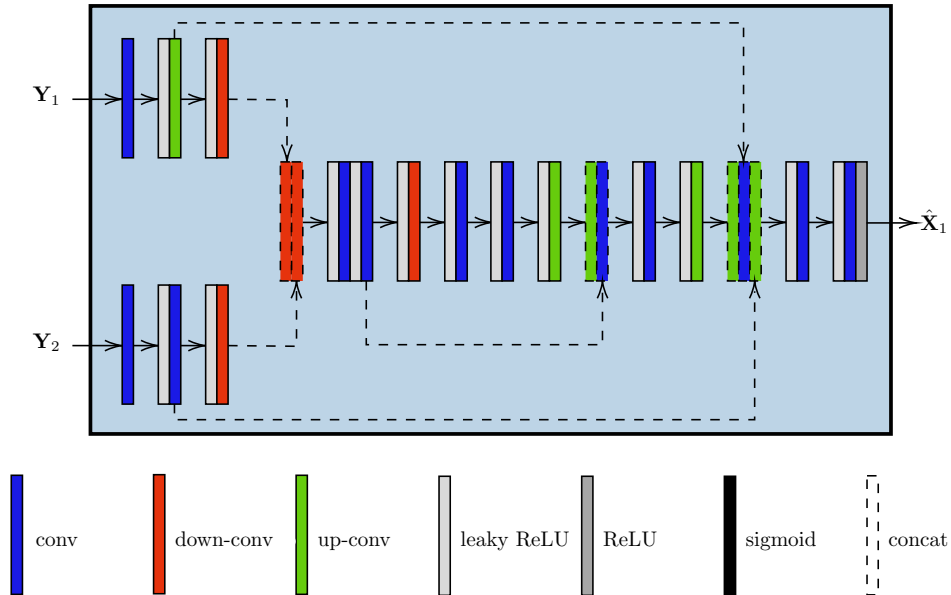


Fig. 2. Architecture of the generative networks.

Regarding the network $C(\cdot, \cdot; \Theta_C)$ dedicated to CI inference, it basically performs a mapping with the same input and target spaces as the fusion network detailed above. Even if the respective underlying tasks are different (i.e., CD vs. fusion), their objectives are similar, e.g., extracting relevant spatial-spectral information from a pair of images of different spatial and spectral resolutions to produce a HRHS (latent or change) image. Thus, it is quite legitimate to adopt a similar architecture for $C(\cdot, \cdot; \Theta_C)$ as $F(\cdot, \cdot; \Theta_F)$. The only difference lies in the last layer: the ReLU layer has been removed since the CI is not necessarily nonnegative.

Finally, the discriminative network $D(\cdot; \Theta_D)$ takes an LRHS image as an input, that could be the predicted image \hat{Y}_1 or the observed image \hat{Y}_1 , to provide a binary decision. As depicted in Fig. 3, it consists of three down-convolution layers and two flat convolution layers. The network ends with

a sigmoid-based activation layer.

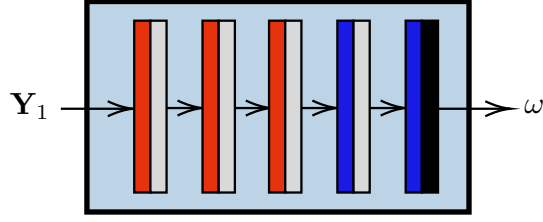


Fig. 3. Architecture of the discriminative network.

IV. EXPERIMENTS ON SIMULATED DATA SETS

This section aims at assessing the efficiency of the proposed robust fusion-based CD-GAN framework by reporting experiments conducted on synthetic data and comparing its performance to those obtained by standard and state-of-the-art CD techniques. In this perspective, the proposed framework is instantiated for the particular case of complementary acquisitions. More precisely, throughout this section the observed images denoted Y_1 will refer to an HS images of low spatial resolution while Y_2 will refer to MS images of higher spatial resolution.

A. Synthetic data generation

In practice, it is generally difficult to obtain couples of multiband images of different resolutions, acquired over the same spatial spot at different time instants, with changed areas sufficiently well located to produce ground truth change maps required to statistically assess the performance of CD methods. Thus the first set of experiments reported in what follows have been conducted following the simulation protocol proposed in [18]. This protocol relies on the availability of a single HRHS image denoted X_{ref} to generate pairs of observed³ HRLS and LRHS images through an unmixing-upmixing process. This process allows the observed images to be affected by physically-inspired thus realistic changes whose maps are predefined and can be resorted to evaluate the performance of the CD methods. The successive steps of this protocol are briefly sketched below. Interested readers are invited to consult [18] for more details.

Generation of HRHS images – Three sets of 22 HRHS images have been extracted from three real HS images acquired by the AVIRIS sensors and depicted in Fig. 4. Each reference image denoted by X_{ref} is composed of $m = 224$ spectral bands and are of size 120×120 pixels (i.e., $n = 14400$).

³With a slight abuse of spelling, the HRLS and LRHS images are still referred to as “observed” or “acquired” images although they have been synthetically generated.



Fig. 4. Color composition of the three hyperspectral reference images.

The resulting 66 reference images are then processed as follows.

Unmixing – From each reference image \mathbf{X}_{ref} , a set of k endmembers gathered in the $m \times k$ matrix \mathbf{M}_{ref} are extracted using vertex component analysis [45], where the number k of endmembers has been adjusted using Hysime [46]. Based on this set of endmembers, the reference image has been unmixed using SUnSAL [47] to recover a corresponding $k \times n$ abundance matrix \mathbf{A}_{ref} .

Change generation – Three kinds of simulated yet realistic changes are independently applied to the reference abundance matrices \mathbf{A}_{ref} to produce modified abundance matrices denoted \mathbf{A}_{chg} . These three change rules are referred to as *zero abundance* (\mathcal{R}_z), *same abundance* (\mathcal{R}_s) and *block abundance* (\mathcal{R}_b) in the sequel (see [18] for more details). For each reference image, the pixels whose respective abundance vectors have been modified are identified by non-zero values in the predefined reference binary map $\mathbf{d}_{\text{ref}} \in \{0, 1\}^n$.

Upmixing – Pairs $(\mathbf{X}_1, \mathbf{X}_2)$ of HRHS latent images are computed by linearly mixing endmember matrices \mathbf{M}_{ref} with the abundances in \mathbf{A}_{ref} or \mathbf{A}_{chg} . More precisely, these simulated pairs of latent images \mathbf{X}_1 and \mathbf{X}_2 are defined as

$$(\mathbf{X}_1, \mathbf{X}_2) \in \{(\mathbf{M}_{\text{ref}}\mathbf{A}_{\text{ref}}, \mathbf{M}_{\text{ref}}\mathbf{A}_{\text{chg}}), (\mathbf{M}_{\text{ref}}\mathbf{A}_{\text{chg}}, \mathbf{M}_{\text{ref}}\mathbf{A}_{\text{ref}})\}. \quad (19)$$

Generation of observed images – Given the HRHS latent images \mathbf{X}_1 and \mathbf{X}_2 produced as above, respective pairs $(\mathbf{Y}_1, \mathbf{Y}_2)$ of observed images are generated according to the forward models (2). In these experiments, as stated above, the observed images are assumed to be of complementary resolutions. Thus the spatial degradation operator $\mathcal{H}_1(\cdot)$ is chosen as a spatially-invariant Gaussian blur with standard deviation $\sigma = 2.35$ followed by a regular down-sampling in both directions of factor 4 leading to $\Delta n = 16$. The spectral degradation operator $\mathcal{H}_1(\cdot)$ mimics the response of a MS

sensor by averaging four contiguous bands along the spectral dimension.

Finally, with the above steps, 440 pairs of images have been generated, from which 418 pairs have been used for training, and the other for testing.

B. Experimental settings

The proposed CD-GAN architecture is implemented using the PyTorch framework on a computer equipped with a Quadro RTX 6000 GPU. Unless otherwise stated, the hyperparameters adjusting the terms associated with the prediction and the spatial regularizations in the loss function (16) have been set to $\alpha = 1$ and $\beta = 10^{-3}$. During the training, Adam [48] is considered as the optimizer with an initial learning rate set to 2×10^{-4} over 15 epochs and batches composed of 4 training samples. These parameters have been adopted for all experiments reported in what follows. The change maps estimated by the proposed method is denoted as $\hat{\mathbf{d}}_{\text{CD-GAN}}$.

Compared methods – The proposed method is compared to four other algorithms. Since very few works considered the problem of CD between images of different resolutions, most of the compared methods consists in applying independent preprocessing to the observed images to reach spatial and spectral resolutions which make a pixel-wise comparison possible. The last method is specifically dedicated to the case of complementary acquisitions.

- The first method consists in band-wisely applying the superresolution algorithm proposed in [49] to the observed image \mathbf{Y}_1 which is subsequently spectrally degraded by applying the operator $\mathcal{H}_2(\cdot)$. The resulting HRLS image can then be pixel-wisely compared to the observed image \mathbf{Y}_2 since they share the same spatial and spectral resolutions. The estimated HR change map $\hat{\mathbf{d}}_{\text{HRLS}}$ is thus obtained by conducting the spatially regularized version of change vector analysis (sCVA) [50].
- The second method applies the same principles with a reverse order of the operator. The observed image \mathbf{Y}_1 is first spectrally degraded following $\mathcal{H}_2(\cdot)$ and then spatially superresolved using the method in [49]. The pair composed of the resulting HRLS image and the observed image \mathbf{Y}_2 is then analyzed using sCVA to produce a HR change map denoted $\hat{\mathbf{d}}_{\text{LSHR}}$.
- The observed image \mathbf{Y}_1 is spectrally degraded following $\mathcal{H}_2(\cdot)$ while the observed image \mathbf{Y}_2 is spatially degraded following $\mathcal{H}_1(\cdot)$. The pair of resulting LRLS images are then compared using sCVA to derive a LR change map denoted as $\hat{\mathbf{d}}_{\text{LRLS}}$.
- The fusion-based CD method proposed in [18] is implemented to estimate a LR change map denoted $\hat{\mathbf{d}}_{\text{F}}$.

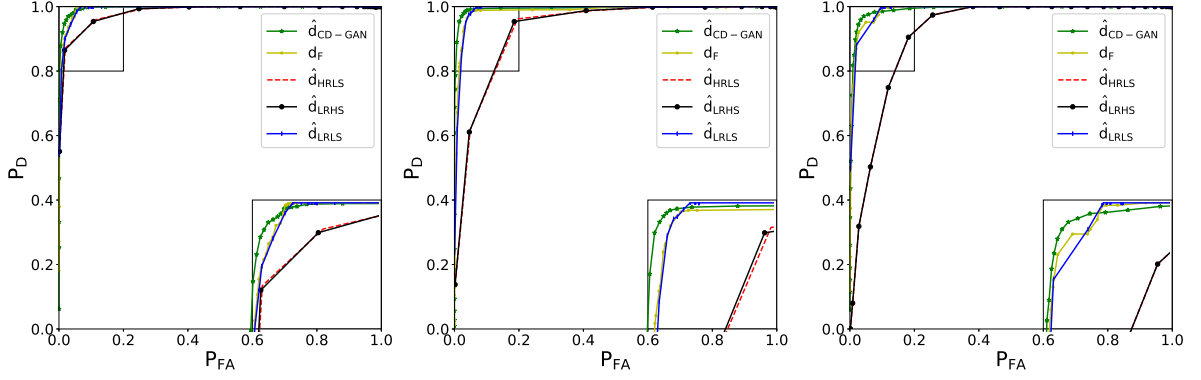


Fig. 5. ROC curves obtained by the compared CD methods for the three change rules: R_b (left), R_s (middle) and R_z (right).

Figures-of-merit – To quantitatively evaluate the performance of the CD methods, the estimated change maps $\hat{\mathbf{d}}$ are compared to the reference change map \mathbf{d}_{ref} to derive the empirical receiver operating characteristics (ROC). ROC curves represent the pixel-wise probability of good detection P_D as a function of the probability of false alarm P_{FA} . They are the privileged and suitable figure-of-merit when assessing the performance of detection methods [51]. Contrary to classification-oriented metrics, they provide a comprehensive description of the expected performance for all functioning points of the detectors. Indeed, as a single graph, they avoid to determine a decision threshold beforehand, which is application-dependent since this threshold directly sets the trade-off between good detections and false alarms. Two quantitative metrics are also derived from these ROC curves, namely the area under the curve (AUC), sometimes referred to as the c-statistic [52, Chap. 9], and the distance (dist.) between the no detection point and the point at the interception of the ROC curve. For both metrics, the closer the values are to 1, the better the CD methods.

Performance comparison – The ROC curves obtained by the compared methods are shown in Fig. 5, for the three change rules R_b , R_s and R_z . The associated quantitative results are reported in Table I. Clearly, these first results show the superiority of the proposed CD-GAN framework when compared to the four other CD methods. More precisely, CD-GAN provides better detections even for very low probability of false alarm, i.e., for exacting functioning point of the detectors. Change maps $\hat{\mathbf{d}}_{\text{HRLS}}$ and $\hat{\mathbf{d}}_{\text{LRLS}}$ behave worst for almost all cases. Note that the estimated change maps $\hat{\mathbf{d}}_{\text{LRLS}}$ and $\hat{\mathbf{d}}_{\text{F}}$ are defined at low spatial resolutions, contrary to the three other methods.

Sensitivity analysis – We now discuss the impact of the hyperparameter β adjusting the weight of the spatial sparsity-inducing regularization in the loss function (16). Table II reports the quantitative results associated with the three change rules R_z , R_s and R_b for values of β in the set $\{0, 10^{-4}, 10^{-3}, 10^{-2}\}$. Optimal values are highlighted in bold. These empirical results demonstrates the interest of incorporating this spatial regularization since the case $\beta = 0$, i.e., with no regularization,

TABLE I
PERFORMANCE COMPARISON: QUANTITATIVE DETECTION PERFORMANCE.

		$\hat{\mathbf{d}}_{\text{CD-GAN}}$	$\hat{\mathbf{d}}_{\text{F}}$	$\hat{\mathbf{d}}_{\text{HRLS}}$	$\hat{\mathbf{d}}_{\text{LSHR}}$	$\hat{\mathbf{d}}_{\text{LRLS}}$
R_b	AUC	0.9962	0.9937	0.9811	0.9811	0.9927
	Dist.	0.9774	0.9650	0.9593	0.9537	0.9446
R_s	AUC	0.9952	0.9844	0.9688	0.9693	0.9891
	Dist.	0.9734	0.9513	0.9289	0.9164	0.9401
R_z	AUC	0.9949	0.9842	0.9816	0.9816	0.9706
	Dist.	0.9758	0.8992	0.9457	0.9457	0.9622

leads to the worst detection performance. Conversely, for a quite wide range of non-zero values of β , i.e., $\beta \in \{10^{-4}, 10^{-3}, 10^{-2}\}$, the detection performance clearly improves with optimal performance obtained for $\beta = 10^{-3}$, which is the default value chosen for the experiments reported in this section.

TABLE II
SENSITIVITY ANALYSIS W.R.T. THE HYPERPARAMETER β : QUANTITATIVE DETECTION PERFORMANCE.

		$\beta = 0$	$\beta = 10^{-4}$	$\beta = 10^{-3}$	$\beta = 10^{-2}$
R_b	AUC	0.9335	0.9925	0.9962	0.9950
	Dist.	0.8357	0.9688	0.9774	0.9651
R_s	AUC	0.8399	0.9835	0.9952	0.9896
	Dist.	0.7892	0.9601	0.9734	0.9560
R_z	AUC	0.8854	0.9768	0.9949	0.9937
	Dist.	0.8534	0.9350	0.9758	0.9684

Note that a similar analysis has been conducted for the hyperparameter α adjusting the weight of the prediction term in the overall loss (16). The results, which show the limited impact of this hyperparameter on the detection performance, are not reported herein for brevity.

Impact of the fusion methods – In the proposed CD-GAN framework, the fusion network $F(\cdot, \cdot; \Theta_F)$

can be chosen by the end-user and has been assumed to be trained beforehand. Section III-C provides the detailed architectures adopted in most of the experiments discussed herein. As stated before, it heavily relies on the PS-GAN architecture proposed in [40]. To illustrate the versatility of the proposed framework, we propose to instantiate the proposed framework with another fusion network, namely the deep blind hyperspectral image fusion (DBIN) proposed in [41]. Besides, as a complementary analysis, we consider a semi-supervised scenario where the latent image \mathbf{X}_1 (i.e., the HRHS image associated with the observed image \mathbf{Y}_1) is also available for training. Note that this more favorable scenario is the one considered in [40] to train PS-GAN. In this case, the discriminative network $D(\cdot; \Theta_D)$ and the prediction loss (14) can be easily adapted accordingly to distinguish the estimated fused image $\hat{\mathbf{X}}_1$ from the true latent image \mathbf{X}_1 . The quantitative metrics are reported in Table III for the three implemented change rules. These results show that, whatever the adopted fusion network, the proposed unsupervised CD-GAN framework reaches detection performance comparable to the one obtained in a semi-supervised scenario. In addition, they show that the proposed CD framework is quite robust to the choice of the fusion method.

TABLE III
IMPACT OF THE FUSION METHOD: QUANTITATIVE DETECTION PERFORMANCE.

		CD-GAN		Semi-supervised
		DBIN	PS-GAN	CD-GAN
R_b	AUC	0.9860	0.9962	0.9971
	Dist.	0.9650	0.9774	0.9774
R_s	AUC	0.9933	0.9952	0.9946
	Dist.	0.9750	0.9734	0.9737
R_z	AUC	0.9975	0.9949	0.9940
	Dist.	0.9849	0.9758	0.9851

Robustness w.r.t. the forward models – The proposed framework sketched in Fig. 1 requires the definition of the spatial and spectral degradation operators $\mathcal{H}_1(\cdot)$ and $\mathcal{H}_2(\cdot)$. In some practical applications, one may have only a partial knowledge regarding these operators related to the sensors. Experiments have been conducted to assess the robustness of the proposed CD-GAN framework w.r.t. to model mismatch. More precisely, first the CD-GAN architecture has been trained with corrupted

degradation operators on a training set composed of observed images generated with uncorrupted degradation operators and following the protocol described in Section IV-A. Then, with all network parameters fixed, the corrupted operators have been updated in a second training procedure. Finally, the CD-GAN has been trained a second time based on these corrected operators. Regarding the corruption processes, the spatial degradation operator $\mathcal{H}_1(\cdot)$ specified in Section IV-A has been replaced by a spatially-invariant Gaussian blur with standard deviation $\sigma = 1.70$. Inspired by the study conducted in [38], the spectral filters which compose the spectral degradation operator $\mathcal{H}_2(\cdot)$ have been corrupted by an additive zero-mean Gaussian noise with a variance leading to a $\text{SNR} = 8\text{dB}$.

TABLE IV
ROBUSTNESS W.R.T. FORWARD MODELS: QUANTITATIVE DETECTION PERFORMANCE.

		$\hat{d}_{\text{CD-GAN}}$	\hat{d}_{F}	\hat{d}_{HRLS}	\hat{d}_{LSHR}	\hat{d}_{LRLS}
R_b	AUC	0.9948	0.9936	0.9254	0.9302	0.9371
	Dist.	0.9714	0.9723	0.8766	0.8747	0.9116
R_s	AUC	0.9918	0.9842	0.9788	0.9781	0.9656
	Dist.	0.9625	0.9513	0.9613	0.9613	0.9201
R_z	AUC	0.9984	0.9842	0.9219	0.9128	0.6927
	Dist.	0.9844	0.8992	0.8759	0.8759	0.6744

Table IV reports the quantitative results obtained by the compared methods. They show that the proposed CD-GAN obtain higher metrics than those obtained by the compared methods. In conclusion, when compared with other methods, the proposed CD-GAN framework is shown to be robust w.r.t. to the misspecification of the degradation operators for the three implemented change rules.

V. EXPERIMENTS ON REAL DATA SETS

For an illustrative purpose, complementary experiments have been conducted on a real data set, namely the Santa Barbara data set. It is composed of two HS images acquired by the AVIRIS sensor in 2013 and 2014, respectively, to monitor the change of composition over Santa Barbara area in California [53]. These images are composed of 984×740 pixels, with $m = 224$ spectral bands. In the experiments, two HRHS sub-images of sizes of 120×120 are selected. The spatial and spectral degradation operators $\mathcal{H}_1(\cdot)$ and $\mathcal{H}_2(\cdot)$ detailed in Section IV-A are applied to each of these HRHS images to mimic heterogeneous acquisitions with complementary resolutions, i.e., producing one

HRLS image and one LRHS image. The HRLS and LRHS images as well as the actual binary CMs constituting the two data sets, denoted SB1 and SB2, are shown in Fig. 6.

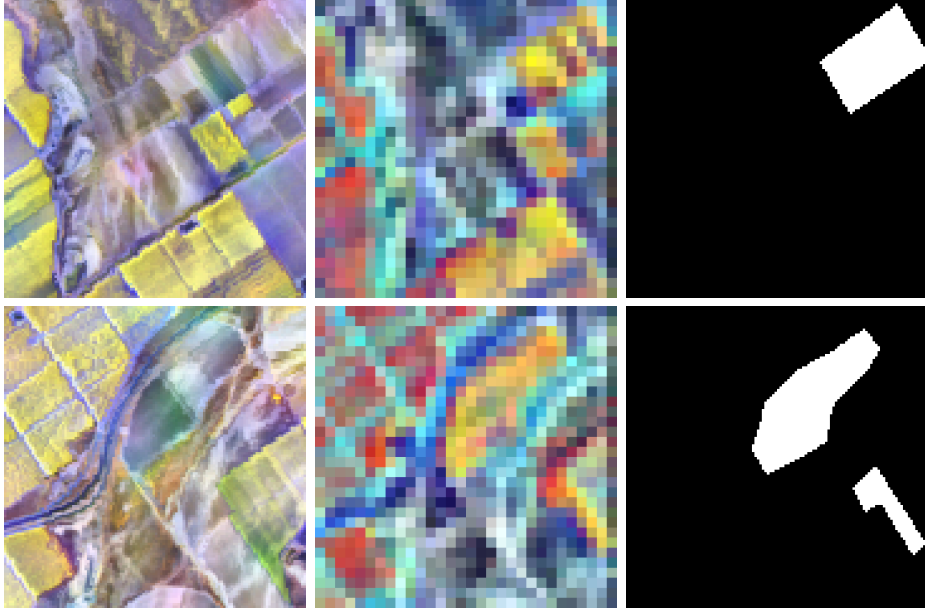


Fig. 6. Data sets SB1 (top) and SB2 (bottom): color composition of the HRLS observed image (left), color composition of the LRHS observed image (middle) and the binary CM (right) where white (resp. black) pixels correspond to changed (resp. unchanged) areas.

Regarding the data set SB1, the CIs and the resulting binary CMs recovered by the compared methods are shown in Fig. 7. Visual inspection allows one to state that recovering the changed areas between the two observed images is a challenging task for all compared methods. The estimated change map \hat{d}_F does not succeed in identifying the changed regions accurately, which leads to a large number of actually changed pixels to be detected as unchanged. The change maps \hat{d}_{HRLS} and \hat{d}_{LSHR} seem to preserve more changed pixels but at the price of leading to a lot of false alarms since a large number of actually unchanged pixels are detected as changed. The estimated LRHS CM \hat{d}_{LRLS} is able to locate the major changes and the corresponding estimated CI exhibits a better contrast than the previous methods. However, many isolated unchanged pixels are misclassified and, similarly to the fusion-based map, the CI and CM are of low spatial resolution. Conversely, the results associated with the proposed CD-GAN show accurate detections of the changes with a low number of false alarms. These findings are confirmed by the ROC curves depicted in Fig. 8 (left) and the quantitative results reported in Table V. From Fig. 8 (left), it appears that the proposed CD-GAN provides high detection rate whatever the functioning point of the detector (i.e., for all values of PFA). From a quantitative point-of-view, the proposed CD-GAN framework obtains higher dist. score and AUC.

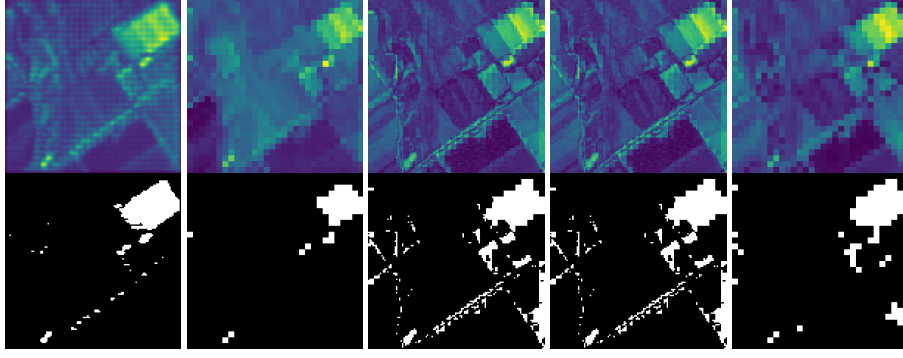


Fig. 7. Data set SB1: CI (top) and CM (bottom) estimated by the compared methods with, from left to right: \hat{d}_{CD-GAN} , \hat{d}_F , \hat{d}_{HRLS} , \hat{d}_{LSHR} , \hat{d}_{LRLS} .

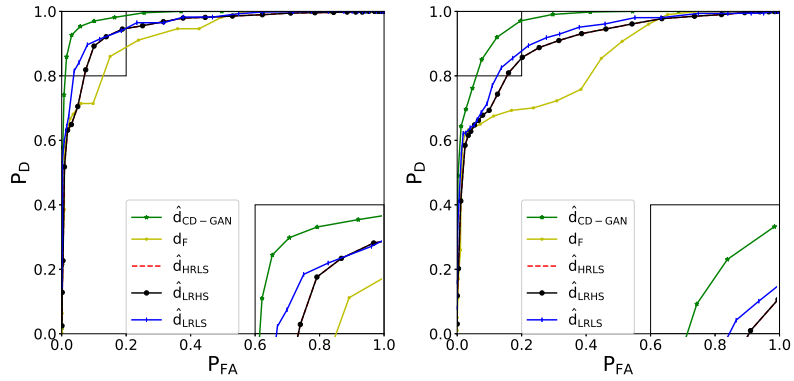


Fig. 8. Data sets SB1 (left) and SB2 (right): ROC curves obtained by the compared methods.

TABLE V

DATA SETS SB1 AND SB2: QUANTITATIVE DETECTION PERFORMANCE.

		\hat{d}_{CD-GAN}	\hat{d}_F	\hat{d}_{HRLS}	\hat{d}_{LSHR}	\hat{d}_{LRLS}
SB1	AUC	0.9867	0.921	0.9496	0.9498	0.9618
	Dist.	0.9534	0.8602	0.8923	0.8923	0.8964
SB2	AUC	0.9660	0.8479	0.9033	0.9033	0.9207
	Dist.	0.9196	0.7225	0.8091	0.8091	0.8549

Regarding the data set SB2, the CI and CM estimated by the compared methods are shown in Fig. 9. The change maps derived from the HRLS and LSHR CI are composed of many isolated pixels wrongly detected as changed. This may be due to the superresolution operation which is sensitive to noise. The estimated LRLS CM seems to achieve better performance, although changes in some

areas are not well detected due to the loss of useful information induced by the underlying spectral and spatial degradations. Compared to these previous methods, the fusion-based CD method presents misclassified areas of change, but the result remains still visually unsatisfactory. The change map estimated by the proposed CD-GAN framework is composed of more well located changed pixels, with a significant reduction of false alarms. This visual inspection is confirmed by the quantitative results reported in Table V where the proposed CD-GAN framework reaches higher metrics (AUC and dist.) than the compared methods. The ROC curves depicted in Fig. 8 (right) show that the CD-GAN strategy provides better detection whatever the functioning point of the detector, i.e., for a wide range of rate of false alarms.

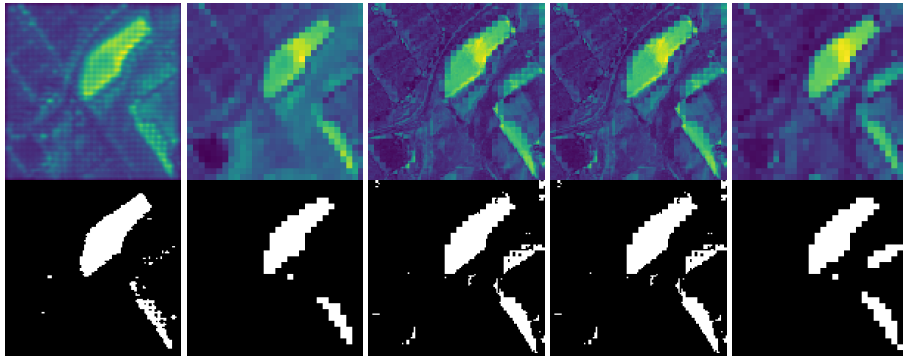


Fig. 9. Data set SB2: CI (top) and CM (bottom) estimated by the compared methods with, from left to right: $\hat{d}_{\text{CD-GAN}}$, \hat{d}_{F} , \hat{d}_{HRLS} , \hat{d}_{LSHR} , \hat{d}_{LRLS} .

VI. CONCLUSION

This paper introduced a robust fusion-based adversarial framework for detecting changes between heterogeneous images in an unsupervised scenario. The proposed approach capitalized on the availability of a predefined and previously trained fusion network. Following a robust fusion-based change detection strategy, this network was complemented with an additional network of the same architecture specifically dedicated to detect change between images of possibly different spatial and spectral resolutions. The overall architecture was trained within an adversarial paradigm, enriching the canonical adversarial loss function with task-driven terms. Experiments conducted on simulated and real data sets illustrated the efficiency, the versatility and the robustness of the proposed change detection framework.

ACKNOWLEDGEMENTS

The authors would like to thank Florentin Coeurdoux (IRIT, University of Toulouse) for his relevant advice regarding the practical implementation of the proposed CD-GAN architecture.

REFERENCES

- [1] A. P. Tewkesbury, A. J. Comber, N. J. Tate, A. Lamb, and P. F. Fisher, "A critical synthesis of remotely sensed optical image change detection techniques," *Remote Sens. Environment*, vol. 160, pp. 1–14, 2015.
- [2] L. Bruzzone and F. Bovolo, "A novel framework for the design of change-detection systems for very-high-resolution remote sensing images," *Proc. IEEE*, vol. 101, no. 3, pp. 609–630, 2012.
- [3] L. Gueguen and R. Hamid, "Toward a generalizable image representation for large-scale change detection: Application to generic damage analysis," *IEEE Trans. Geosci. Remote Sens.*, vol. 54, no. 6, pp. 3378–3387, 2016.
- [4] I. R. Hegazy and M. R. Kaloop, "Monitoring urban growth and land use change detection with GIS and remote sensing techniques in Daqahlia governorate Egypt," *Int. J. Sustainable Built Environment*, vol. 4, no. 1, pp. 117–124, 2015.
- [5] F. Wang and Y. J. Xu, "Comparison of remote sensing change detection techniques for assessing hurricane damage to forests," *Environmental monitoring and assessment*, vol. 162, no. 1, pp. 311–326, 2010.
- [6] R. Manonmani and G. Suganya, "Remote sensing and GIS application in change detection study in urban zone using multi temporal satellite," *Int. J. Geomatics and Geosci.*, vol. 1, no. 1, pp. 60–65, 2010.
- [7] Y. Sun, L. Lei, X. Li, X. Tan, and G. Kuang, "Patch similarity graph matrix-based unsupervised remote sensing change detection with homogeneous and heterogeneous sensors," *IEEE Trans. Geosci. Remote Sens.*, vol. 59, no. 6, pp. 4841–4861, 2020.
- [8] L. Bruzzone and D. F. Prieto, "An adaptive semiparametric and context-based approach to unsupervised change detection in multitemporal remote-sensing images," *IEEE Trans. Image Process.*, vol. 11, no. 4, pp. 452–466, 2002.
- [9] Z. Li, W. Shi, H. Zhang, and M. Hao, "Change detection based on gabor wavelet features for very high resolution remote sensing images," *IEEE Geosci. Remote Sens. Lett.*, vol. 14, no. 5, pp. 783–787, 2017.
- [10] F. Gao, J. Dong, B. Li, and Q. Xu, "Automatic change detection in synthetic aperture radar images based on PCANet," *IEEE Geosci. Remote Sens. Lett.*, vol. 13, no. 12, pp. 1792–1796, 2016.
- [11] X. Niu, M. Gong, T. Zhan, and Y. Yang, "A conditional adversarial network for change detection in heterogeneous images," *IEEE Geosci. Remote Sens. Lett.*, vol. 16, no. 1, pp. 45–49, 2018.
- [12] W. Zhao, Z. Wang, M. Gong, and J. Liu, "Discriminative feature learning for unsupervised change detection in heterogeneous images based on a coupled neural network," *IEEE Trans. Geosci. Remote Sens.*, vol. 55, no. 12, pp. 7066–7080, 2017.
- [13] H. Li, M. Gong, M. Zhang, and Y. Wu, "Spatially self-paced convolutional networks for change detection in heterogeneous images," *IEEE J. Sel. Topics Appl. Earth Observations Remote Sens.*, vol. 14, pp. 4966–4979, 2021.
- [14] A. A. Nielsen, K. Conradsen, and J. J. Simpson, "Multivariate alteration detection (MAD) and MAF postprocessing in multispectral, bitemporal image data: New approaches to change detection studies," *Remote Sens. Environment*, vol. 64, no. 1, pp. 1–19, 1998.
- [15] A. A. Nielsen, "The regularized iteratively reweighted MAD method for change detection in multi-and hyperspectral data," *IEEE Trans. Image Process.*, vol. 16, no. 2, pp. 463–478, 2007.
- [16] V. Alberga, M. Idrissa, V. Lacroix, and J. Inglada, "Performance estimation of similarity measures of multi-sensor images for change detection applications," in *Proc. IEEE Int. Workshop Analysis Multitemporal Remote Sensing Images (MultiTemp)*. IEEE, 2007, pp. 1–5.
- [17] —, "Comparison of similarity measures of multi-sensor images for change detection applications," in *Proc. IEEE Int. Conf. Geosci. Remote Sens. (IGARSS)*. IEEE, 2007, pp. 2358–2361.
- [18] V. Ferraris, N. Dobigeon, Q. Wei, and M. Chabert, "Detecting changes between optical images of different spatial and spectral resolutions: a fusion-based approach," *IEEE Trans. Geosci. Remote Sens.*, vol. 56, no. 3, pp. 1566–1578, 2017.

- [19] —, “Robust fusion of multi-band images with different spatial and spectral resolutions for change detection,” *IEEE Trans. Comput. Imag.*, vol. 3, no. 2, pp. 175–186, April 2017.
- [20] V. Ferraris, N. Dobigeon, and M. Chabert, “Robust fusion algorithms for unsupervised change detection between multi-band optical images – A comprehensive case study,” *Information Fusion*, vol. 64, pp. 293–317, Dec. 2020.
- [21] J. Liu, M. Gong, K. Qin, and P. Zhang, “A deep convolutional coupling network for change detection based on heterogeneous optical and radar images,” *IEEE Trans. Neural Netw. Learn. Syst.*, vol. 29, no. 3, pp. 545–559, 2016.
- [22] J. Liu, M. Gong, A. K. Qin, and K. C. Tan, “Bipartite differential neural network for unsupervised image change detection,” *IEEE Trans. Neural Netw. Learn. Syst.*, vol. 31, no. 3, pp. 876–890, 2019.
- [23] H. Zhang, M. Lin, G. Yang, and L. Zhang, “Escnet: An end-to-end superpixel-enhanced change detection network for very-high-resolution remote sensing images,” *IEEE Trans. Neural Netw. Learn. Syst.*, 2021.
- [24] Z.-G. Liu, Z.-W. Zhang, Q. Pan, and L.-B. Ning, “Unsupervised change detection from heterogeneous data based on image translation,” *IEEE Trans. Geosci. Remote Sens.*, pp. 1–13, 2021.
- [25] I. Goodfellow, J. Pouget-Abadie, M. Mirza, B. Xu, D. Warde-Farley, S. Ozair, A. Courville, and Y. Bengio, “Generative adversarial nets,” in *Adv. in Neural Information Process. Systems (NIPS)*, vol. 27, 2014.
- [26] P. Isola, J.-Y. Zhu, T. Zhou, and A. A. Efros, “Image-to-image translation with conditional adversarial networks,” in *Proc. Int. Conf. on Computer Vision and Pattern Recognition (CVPR)*, 2017, pp. 1125–1134.
- [27] M. Ravanbakhsh, M. Nabi, E. Sangineto, L. Marcenaro, C. Regazzoni, and N. Sebe, “Abnormal event detection in videos using generative adversarial nets,” in *Proc. IEEE Int. Conf. Image Process. (ICIP)*. IEEE, 2017, pp. 1577–1581.
- [28] Q. Wei, N. Dobigeon, and J.-Y. Tourneret, “Fast fusion of multi-band images based on solving a Sylvester equation,” *IEEE Trans. Image Process.*, vol. 24, no. 11, pp. 4109–4121, 2015.
- [29] R. Dian, S. Li, and X. Kang, “Regularizing hyperspectral and multispectral image fusion by CNN denoiser,” *IEEE Trans. Neural Netw. Learn. Syst.*, vol. 32, no. 3, pp. 1124–1135, 2020.
- [30] Y. Xu, Z. Wu, J. Chanussot, and Z. Wei, “Hyperspectral images super-resolution via learning high-order coupled tensor ring representation,” *IEEE Trans. Neural Netw. Learn. Syst.*, vol. 31, no. 11, pp. 4747–4760, 2020.
- [31] W. Wang, X. Fu, W. Zeng, L. Sun, R. Zhan, Y. Huang, and X. Ding, “Enhanced deep blind hyperspectral image fusion,” *IEEE Trans. Neural Netw. Learn. Syst.*, 2021.
- [32] J.-F. Hu, T.-Z. Huang, L.-J. Deng, T.-X. Jiang, G. Vivone, and J. Chanussot, “Hyperspectral image super-resolution via deep spatospectral attention convolutional neural networks,” *IEEE Trans. Neural Netw. Learn. Syst.*, 2021.
- [33] F. Bovolo and L. Bruzzone, “A theoretical framework for unsupervised change detection based on change vector analysis in the polar domain,” *IEEE Trans. Geosci. Remote Sens.*, vol. 45, no. 1, pp. 218–236, 2006.
- [34] P. Du, X. Wang, D. Chen, S. Liu, C. Lin, and Y. Meng, “An improved change detection approach using tri-temporal logic-verified change vector analysis,” *ISPRS J. Photogramm. Remote Sens.*, vol. 161, pp. 278–293, 2020.
- [35] S. N and V. S, “Image segmentation by using thresholding techniques for medical images,” *Computer Science & Engineering: An Int. Journal*, vol. 6, pp. 1–13, 02 2016.
- [36] G. Vivone, L. Alparone, J. Chanussot, M. Dalla Mura, A. Garzelli, G. A. Licciardi, R. Restaino, and L. Wald, “A critical comparison among pansharpening algorithms,” *IEEE Trans. Geosci. Remote Sens.*, vol. 53, no. 5, pp. 2565–2586, 2014.
- [37] L. Loncan, L. B. Almeida, J. M. Bioucas-Dias, X. Briottet, J. Chanussot, N. Dobigeon, S. Fabre, W. Liao, G. Licciardi, M. Simoes, J.-Y. Tourneret, M. Veganzones, G. Vivone, Q. Wei, and N. Yokoya, “Hyperspectral pansharpening: a review,” *IEEE Geosci. Remote Sens. Mag.*, vol. 3, no. 3, pp. 27–46, Sept. 2015.
- [38] Q. Wei, N. Dobigeon, and J.-Y. Tourneret, “Bayesian fusion of multi-band images,” *IEEE J. Sel. Topics Signal Process.*, vol. 9, no. 6, pp. 1117–1127, Sept. 2015.
- [39] L. Wald, T. Ranchin, and M. Mangolini, “Fusion of satellite images of different spatial resolutions: Assessing the quality of resulting images,” *Photogrammetric Engineering Remote Sens.*, vol. 63, no. 6, pp. 691–699, 1997.

- [40] Q. Liu, H. Zhou, Q. Xu, X. Liu, and Y. Wang, “Psgan: A generative adversarial network for remote sensing image pan-sharpening,” *IEEE Trans. Geosci. Remote Sens.*, 2020.
- [41] W. Wang, W. Zeng, Y. Huang, X. Ding, and J. Paisley, “Deep blind hyperspectral image fusion,” in *Proc. IEEE Int. Conf. Computer Vision (ICCV)*, 2019, pp. 4150–4159.
- [42] L. Zhang, J. Nie, W. Wei, Y. Li, and Y. Zhang, “Deep blind hyperspectral image super-resolution,” *IEEE Trans. Neural Netw. Learn. Syst.*, vol. 32, no. 6, pp. 2388–2400, 2020.
- [43] A. L. Maas, A. Y. Hannun, A. Y. Ng *et al.*, “Rectifier nonlinearities improve neural network acoustic models,” in *Proc. Int. Conf. Machine Learning (ICML)*, vol. 30, no. 1. Citeseer, 2013, p. 3.
- [44] O. Ronneberger, P. Fischer, and T. Brox, “U-net: Convolutional networks for biomedical image segmentation,” in *Int. Conf. Medical image Computing and Computer-Assisted Intervention (MICCAI)*. Springer, 2015, pp. 234–241.
- [45] J. Nascimento and J. Dias, “Vertex component analysis: a fast algorithm to unmix hyperspectral data,” *IEEE Trans. Geosci. Remote Sens.*, vol. 43, no. 4, pp. 898–910, 2005.
- [46] J. Nascimento and J. M. Bioucas-Dias, “Hyperspectral signal subspace estimation,” in *Proc. IEEE Int. Conf. Geosci. Remote Sens. (IGARSS)*, 2007, pp. 3225–3228.
- [47] M.-D. Iordache, J. M. Bioucas-Dias, and A. Plaza, “Sparse unmixing of hyperspectral data,” *IEEE Trans. Geosci. Remote Sens.*, vol. 49, no. 6, pp. 2014–2039, 2011.
- [48] D. Kingma and J. Ba, “Adam: A method for stochastic optimization,” *Proc. IEEE Int. Conf. Learn. Represent. (ICLR)*, 2014.
- [49] N. Zhao, Q. Wei, A. Basarab, N. Dobigeon, D. Kouamé, and J.-Y. Tournier, “Fast single image super-resolution using a new analytical solution for $\ell_2 - \ell_2$ problems,” *IEEE Trans. Image Process.*, vol. 25, no. 8, pp. 3683–3697, 2016.
- [50] R. D. Johnson and E. Kasischke, “Change vector analysis: A technique for the multispectral monitoring of land cover and condition,” *Int. J. Remote Sensing*, vol. 19, no. 3, pp. 411–426, 1998.
- [51] M. S. Pepe, “Receiver operating characteristic methodology,” *J. Amer. Stat. Assoc.*, vol. 95, no. 449, pp. 308–311, March 2000.
- [52] T. Hastie, R. Tibshirani, and J. H. Friedman, *The elements of statistical learning: data mining, inference, and prediction*, 2nd ed. New York: Springer, 2009.
- [53] A. Shafique, G. Cao, Z. Khan, M. Asad, and M. Aslam, “Deep learning-based change detection in remote sensing images: A review,” *Remote Sens.*, vol. 14, no. 4, p. 871, 2022.